Supplementary Materials for

"Oscillating paramagnetic Meissner effect and Berezinskii–Kosterlitz–Thouless transition in $Bi_2Sr_2CaCu_2O_{8+\delta}$ monolayer"

This file includes:

I. **Materials and Methods**

II. **Supplementary Text**

III. **Figs. S1 to S10**

I. Materials and Methods

1. Fabrication and characterization of ultrathin samples

We followed the previous procedure to fabricate monolayer and multilayer Bi2212 and $NbSe_2$ flake samples. We determined the thickness of the prepared sample by atomic force microscopy (Fig. S1) and established a calibration of the thickness and optical contrast. Since the monolayer and ultrathin samples for sSQUID measurements had to be capped by hBN immediately after fabrication, we used their optical image to determine the thickness.

The bulk crystal showed diamagnetic response at 88 K as measured by a commercial vibrating sample magnetometer (Fig. S2a). This was consistent with the T_C = 88.2 K measured by sSQUID of a thick flake sample exfoliated from the sample ingot and was close to the optimal T_C of Bi2212. The diamagnetic moment reduced as a function of increasing external field (Fig. S2b). However, no paramagnetic signal was visible in such bulk measurements.

2. Scanning SQUID magnetometry and susceptometry

Scanning SQUID measurements were performed in a closed-cycle He-4 refrigerator. The SQUID sensors used for this study were scanning 2-junction SQUID susceptometers with two balanced pickup loops of 0.5 or 3 μm diameter in a gradiometric configuration, each surrounded by a one-turn field coils of 5 or 7.5 μm diameter. These devices were planarized throughout, which minimized the spacing between the pickup loop-field coil pair and the sample surface. The spatial resolution was limited by both the size of the pickup loop and the height of it from the sample.

For the scanning SQUID measurements throughout this paper, we employed three different modes to probe electronic and magnetic properties [18]. Magnetometry (Φ) was a DC measurement of flux through the pickup loop as a function of position and shows the intrinsic magnetization of the sample; susceptometry ($d\Phi/dI_F$) measured the inductive response of the sample through the pickup loop to a modulation current in the field coil I_F; current magnetometry (Φ_I'/I_{AC}) was performed with a lock-in measurement of the in-phase component of the flux Φ_I' generated by an applied AC current I_{AC} (typically around 504 Hz) flowing through the sample. The magnetometry was performed simultaneously with susceptometry or current magnetometry. Because the pickup loop was parallel to the sample surface, it was only sensitive to the local out-of-plane magnetic field. The maximum I_F was limited by the critical current of the superconducting planar wires of the coil. The maximum out-of-plane magnetic field at the centre of a current loop with 30 mA of current and 5 μm diameter was about 30 mG.

II. Supplementary Text

1. Estimate Pearl length and superfluid density from susceptometry

We used Pearl length Λ to characterize the diamagnetic length scale of a weakly diamagnetic film, whose thickness was much less than the London penetration depth. From scanning SQUID susceptometry, Λ was related to real part of the susceptibility χ' as: $\chi'/\chi_s = -a/\Lambda(1-\frac{2\bar{z}}{\sqrt{1+4\bar{z}^2}})$, where $\chi_s = 490\ \Phi_0/A$ was the self-inductance, $a = 5$ μm was the radius of the field coil and $\bar{z} = z/a$. Fitting the touch-down curve as shown in Figure 1b using the above equation, we obtained Λ of the monolayer was 171 μm.

Besides the relation mentioned in the main text, $1/\Lambda$ was also proportional to the sheet superfluid density $\rho_s^{2D} = \rho_s t$ following the relation [19]: $\rho_s^{2D} = \frac{2m_e^*}{\mu_0 e^* \Lambda}$ where m_e^* and e^* were the mass and charge of the Cooper pair and μ_0 was the vacuum permeability.

2. Additional data on different samples

1) Monolayer Bi2212

Firstly, the peak positions in H (H_p) of χ'(H, T) did not depend on whether H or T was swept (Fig. S3). However, the amplitude of the peaks did depend on the history, which could be seen from a much-reduced contrast of peak '2' (Fig. S3).

We observed similarly sharp PME peaks at the triangle-shaped region of the monolayer (Fig. 1g), which had a lower T_C = 52 K than the diamond and the rectangular-shaped regions (Fig. S4a). However, there were more orders of the peaks visible (Fig. S4b) and the spacing between the peaks was smaller than that of the left diamond-shaped domain (Fig. 3b). This suggested that the triangle-region had a larger domain size than the diamond-shaped domain. As the overall size of the diamond-shaped domain was only a small fraction of the whole sample (compare Fig. 1g and Fig. 1c), we speculate that the triangle-shaped domain was actually composed of the perimeter of the sample which surrounded the diamond and the rectangular domains. This was reasonable because the perimeter of the sample tended to lose more oxygen during the fabrication process and therefore had a lower T_C than the interior.

Changing the modulation frequency in the low frequency regime did not affect H_p (Fig. S5a). This ruled out the PME peaks as a coincidental resonance peak from the AC measurement. The amplitude of the peaks reduced with increasing frequency. Since the peaks only occurred at quantized flux, increasing the modulation frequency smeared out the point of the phase coherence and therefore reduced the amplitude of the peaks. This observation also suggested that the PME peaks would be even stronger in the zero-frequency limit. The H_p also did not depend on the modulation amplitude when the modulation current was less than 0.15 mA (Fig. S5b). However, when the current was over 0.4 mA the peaks were again smeared out (Fig. S5c). This could similarly be explained by the phase coherence condition being compromised as the modulation flux was comparable to the overall phase in the domain.

2) Quadruple-layer Bi2212

For a quadruple-layer Bi2212 sample (8 nm thick), we observed in the magnetometry image isolated vortices as well as flux contrast at the edge of the sample due to the circulating Meissner current after it was field cooled and measured under 117 mG at 10 K (Fig. S6). The large size of the vortices in the magnetometry image is a reflection of its Pearl length, estimated to be ~ 10 μm from the approach curve. The susceptibility was diamagnetic over the entire sample and no normal core was visible (Fig. S6b) as its coherence length of ~ 2 nm was 3 orders of magnitude smaller than the diameter of the pickup loop.

What was different was that single vortex could be trapped and resolved in the multi-layers. This allowed us to further confirm a deep connection between the paramagnetic response and the quantized flux instead of the field. When there was no trapped vortex and only a very small field was applied (Fig. S6c), there was little paramagnetic region in χ’ even at 82 K (Fig. S6d).

However, after we performed a field cooling to trap a single vortex in the middle of the sample (Fig. S6e), paramagnetic contrast appeared under zero applied field at the same location as the vortex (Fig. S6e). Again, such paramagnetic signal in susceptibility was not a result of the measurement of the spatially varying flux signal because much stronger flux gradient at lower temperatures did not lead to any paramagnetic signal. Rather, it was an intrinsic paramagnetic response of that particular domain when there was a vortex present.

At a different location on this quadruple-layer sample close to its middle (Fig. S6f), The T_C of this area was about 0.5 K lower than the one from the upper-right part of the sample (Fig. 4a). We observed a slightly different $\chi'(H, T)$ pattern (Fig. S7a) than the latter. Nevertheless, the qualitative feature remained the same that the oscillating PME separated into two different temperature regimes, above and below 84.9 K respectively. The zero-field $\chi'(T)$, proportional to the phase stiffness, also exhibited a kink at this temperature (Fig. S7b). These two features in the multilayers were fundamentally different from the behavior of the monolayer and suggested its origin from the interlayer coupling.

3) 20-nm Bi2212

As the sample got even thicker, the variation of the size of the domains from each layer became more significant. This resulted in more sporadic appearance of the PME peaks as can be seen from the $\chi'(H, T)$ data of the 20-nm thick sample (Fig. S7c). The height of the peaks reduced and the width in H was broadened comparing with those of the thinner samples. This suggested that the contribution to susceptibility from each layer was not in phase due to the difference in domain size. Such a tendency continued with sample thickness and completely smeared out the PME oscillations in the bulk sample, leaving a continuous PME response close to T_C (Fig. 4e).

4) $NbSe_2$ multilayer and bulk sample

First, we show that $NbSe_2$ multilayer did not exhibit any paramagnetic Meissner effect. In the magnetometry image taken at 5 K (Fig. S8a), we could see isolated vortices in this 10 nm thick flake sample. The susceptometry image (Fig. S8b) showed similar amplitude of diamagnetism as a quadruple-layer Bi2212 at low temperature (Fig. S6b). This was consistent with the fact that the bulk $\lambda = 190$ nm of $NbSe_2$ was close to that of optimally-doped Bi2212. The χ'(*H, T*) obtained in the middle of this sample over a similar reduced temperature and field range (Fig. S8c) as that of Bi2212 multilayers showed no paramagnetic peaks. On the other hand, a bulk flake sample (thickness > 200 nm) showed no continuous paramagnetic features at finite *H* as seen in bulk of Bi2212 (Fig. S8d). The zero-field χ'(*T*) of this thick $NbSe_2$ sample was shown in Figure 4f.

3. Simulation of the vortex dynamics using the Coulomb gas model

A Coulomb gas model is defined as the system consisting of particles which have equal magnitude of positive or negative charge. One can apply the two dimensional Coulomb gas model to the superconductor film [8]. In this appendix, we introduce the theoretical analytic method used here. Sec.3.1 describes how to map the two dimensional superconductor to the two dimensional Coulomb gas. The major properties of the two dimensional Coulomb gas are discussed in Sec.3.2. Sec.3.3 contains the steps of the analytic method.

1) Mapping the two dimensional superconductor to the two dimensional Coulomb gas

We begin by giving a heuristic argument for the analogy between the two dimensional superconductor and the two dimensional Coulomb gas [8]. In the following reasoning, we select some formulas from Ginzburg-Landau theory, and for more details, readers can refer to the standard textbook such as [56]. According to Ginzburg-Landau theory, the superconductor film state can be characterized by a complex order parameter: $\psi = \sqrt{\rho(\vec{r})}\,\mathrm{e}^{\mathrm{i}\theta(\vec{r})}$, where $\rho(\vec{r})$ is the superfluid mass density, which we approximate to a constant here, and θ is connected to the superfluid velocity $\vec{v}_s$ by,

$$\vec{v}_s(\vec{r}) = \frac{\hbar}{m^*}\nabla\theta(\vec{r}) - \frac{e^*\vec{A}}{m^*c}, \qquad (1)$$

where $\hbar$ is reduced Planck constant, $m^* = 2m_e$ and $e^* = 2e$ are the mass and charge of a Cooper pair, $\vec{A}$ is gauge vector potential, and c is the speed of light. The energy of the superconductor is proportional to the superfluid velocity squared, i.e., $E^{SF} \propto v_s^2$. The thermal excitations in the superconductor film are vortices, and the integral around a closed loop surrounding vortices of the gradient of the phase $\theta(\vec{r})$ should always be integer multiples of 2π because of the single-valuedness of ψ,

$$\int \mathrm{d}\,\vec{s} \cdot \nabla\theta(\vec{r}) = 2n\pi, \tag{2}$$

where n is an integer. Similarly, the charges in the two dimensional Coulomb gas can excite the electric field, the energy of the electric field is proportional to the electric intensity $\vec{E}$ squared, i.e. $E^{CG} \propto E^2$, and according to the Gauss's theorem, the integral around a closed surface surrounding charged particles of the electric intensity $\vec{E}$ is,

$$\int \mathrm{d}\vec{S} \cdot \vec{E} = 2\pi q, \tag{3}$$

where q is the total charges enclosed by the integral surface. We can set q to be an integer by choosing electrostatic units. Therefore, we can analogize the vortex and the superfluid velocity in the superconductor film to the charged particle and the electric intensity in the Coulomb gas, respectively, except that the electric intensity is perpendicular to the superfluid velocity, namely, $\vec{E} \perp \vec{v}_s$ (see Fig. S9a).

Now we derive the relation between the two dimensional superconductor and the two dimensional Coulomb gas. The relation has been systematically demonstrated in the reference [8], and we outline the main steps of the demonstration here. The Hamiltonian of the system may be expressed as,

$$H_s = \int \mathrm{d}^2\vec{r} \left(\frac{\vec{g}^{\,2}(\vec{r})}{2\rho} + \frac{e^* \vec{A} \cdot \vec{g}(\vec{r})}{2m^* c} \right), \tag{4}$$

where $\vec{g} = \rho(\vec{r})\,\vec{v}_s(\vec{r})$ is the mass current density. Because of considering here how the fluctuations in the superfluid mass current influence the superfluidity, the mass current can be related to a scaler field Φ by,

$$\vec{g}(\vec{r}) = \nabla \times (\Phi(\vec{r})\vec{x}_3) - \frac{\rho e^* \vec{A}}{m^* c}, \tag{5}$$

where the unit vector $\vec{x}_3$ is perpendicular to the plane of the superconductor film. Substituting Eq. (1) and Eq. (5) into Eq. (2), with the help of the Stokes theorem, we finally get the two dimensional Poisson's equation,

$$\nabla^2 \Phi(\vec{r}) = -2\pi n \frac{\rho \hbar}{m^*} \delta(\vec{r}). \tag{6}$$

The two dimensional Poisson's equation can be used to describe the system consisting of particles which have equal magnitude of positive or negative charges, which is usually called “the two dimensional Coulomb gas model”. Therefore, the vortex excited in the superconductor can be recognized as the charged particle in the Coulomb gas, and the scaler field Φ can be recognized as the electrostatic potential. The electric intensity $\vec{E}$ is defined as,

$$\vec{E} = -\nabla \Phi, \tag{7}$$

and the electric current density is defined as,

$$\vec{j} = \frac{e^*}{m^*} \vec{g}. \tag{8}$$

According to Eq. (1) and Eq. (2), the electric intensity is perpendicular to the electric current density, i.e. $\vec{E} \perp \vec{j}$.

2) The two dimensional Coulomb gas model

In this section, we introduce the basic properties of the two dimensional Coulomb gas.

A Coulomb gas model is defined as the system consisting of particles which have equal magnitude of positive or negative charge. The particles interact with each other through the two dimensional Coulomb interaction, described by Poisson's equation,

$$\nabla^2\varphi(\vec{r}) = -2\pi\delta(\vec{r}), \tag{9}$$

where $\varphi(\vec{r})$ is called the two dimensional Coulomb potential. In two dimensions, by solving Eq. (9), the Coulomb potential, induced by a point charge q_i, has logarithmic dependence on the distance $\vec{r}$ to the charge,

$$\varphi_i(\vec{r}) = -q_i \ln(\vec{r}). \tag{10}$$

However, the divergence of the logarithmic function at $\vec{r} = 0, \infty$ is troublesome. To eliminate the singularity, one usually introduces the ultraviolet cutoff σ [57,58] and infrared cutoff λ [59] for the Coulomb potential $\varphi_i(\vec{r})$, corresponding to the vortex core size and the system size for the two dimensional superconductivity, respectively,

$$\varphi_i(\vec{r}) = -q_i \ln\left(\frac{\vec{r}}{\lambda}\right), \tag{11}$$

which means that the distance between the particles can't be less than σ, and the interaction between the particles will be screened if the distance is more than λ. In this case, the self energy E_0 of the point charge q_i can be expressed as,

$$E_0 = -q_i^2 \ln\left(\frac{\sigma}{\lambda}\right). \tag{12}$$

For many-particle systems, the total potential $\varphi(\vec{r})$ at the position $\vec{r}$ is,

$$\varphi(\vec{r}) = \sum_i \varphi_i(\vec{r}), \tag{13}$$

where the sum i is over all particles of the system.

Consider the Hamiltonian of the Coulomb gas system with fluctuations in the number of particles. We denote the number of particles with positive charges, negative charges, and any charges of the system as N^+, N^-, and N, respectively. The Hamiltonian of the system can be divided into electrostatic energy and non-electrostatic energy parts [8]. The non-electrostatic energy part, defined as the chemical potential of the positive (negative) charges $\mu^{+(-)}$, containing the core energy E_c and the difference in excitations for positive and negative charges, denoted by ΔE, can be expressed as [8],

$$\mu^{\pm} = -(E_c \pm \Delta E). \tag{14}$$

The relation between ΔE and the external magnetic field B for the two dimensional superconductivity is [8],

$$\Delta E = \frac{2\pi R^2}{\phi_0} B, \tag{15}$$

where ϕ_0 is the flux quantum. The electrostatic part W_N, i.e., the interaction energy of N particles, according to standard electrodynamics, has the following form,

$$W_N = \frac{1}{2} \iint \vec{E} \cdot \vec{D} \, \mathrm{d}S, \tag{16}$$

where $\vec{E}$ is the electric intensity, and $\vec{D}$ is the electric displacement. To simplify calculation, the Coulomb potential $\varphi(\vec{r})$, namely, Eq. (13), can be used, by the relation to the electric intensity,

$$\vec{E} = -\nabla \varphi. \tag{17}$$

Substituting Eq. (17) to Eq. (16), the electrostatic configuration energy can be expressed,

$$\begin{aligned} W_N &= -\frac{1}{2} \iint \nabla \varphi \cdot \vec{D} \, \mathrm{d}S \\ &= -\frac{1}{2} \iint \nabla \cdot \left(\varphi \vec{D} \right) \mathrm{d}S + \frac{1}{2} \iint \varphi \nabla \cdot \vec{D} \, \mathrm{d}S \\ &= -\frac{1}{2} \oint_b \varphi \vec{D} \cdot \mathrm{d}\vec{l} + \frac{1}{2} \iint \varphi \rho \, \mathrm{d}S, \end{aligned} \tag{18}$$

where the Gauss's theorem and the Maxwell's equation $\nabla \cdot \vec{D} = \rho$ are used, and ρ is the free charge density. Because of the conductor boundary of the system (see Sec. 3.1.3), the charges are distributed on the surface, and their potential is equal, denoted φ_c. Therefore, we can further simplify Eq. (18) into,

$$\begin{aligned} W_N &= -\frac{1}{2} \oint_b \varphi \vec{D} \cdot \mathrm{d}\vec{l} + \frac{1}{2} \iint \varphi \rho \, \mathrm{d}S \\ &= -\frac{1}{2} \varphi_c \oint_b \vec{D} \cdot \mathrm{d}\vec{l} + \frac{1}{2} \iint (\varphi' + \varphi_c) \rho \, \mathrm{d}S \\ &= -\frac{1}{2} \varphi_c Q + \frac{1}{2} \sum_{i=1}^{N} \varphi_i' Q_i + \frac{1}{2} \varphi_c Q \\ &= \frac{1}{2} \sum_{i=1}^{N} \varphi_i Q_i, \end{aligned} \tag{19}$$

where the Gauss law $\oint_b \vec{D}\cdot \mathrm{d}\vec{l} = Q$ is used, and Q are total charges, namely, $Q=\sum_{i=1}^{N} Q_i$. Substituting Eq. (13) into Eq. (19), we can get,

$$W_N = \frac{1}{2}\sum_{i=1}^{N} Q_i \left(\sum_{j=1}^{N} \varphi_j\left(\vec{r}_i\right)\right), \tag{20}$$

noting that $q_i \varphi_i(\vec{r}_i)$ should be replaced by the self energy E_0 using Eq. (12). To sum up, the Hamiltonian of the system consisting of N particles is,

$$H = W_N - N^+\mu^+ - N^-\mu^-. \tag{21}$$

Next, we study the thermodynamic properties of the two dimensional Coulomb gas model. The thermodynamic properties of the system are determined by its partition function Z, which is defined as,

$$Z = \sum_i \int \mathrm{d}\vec{r}_i \frac{\mathrm{e}^{-\beta H}}{N_i^+! N_i^-!}. \tag{22}$$

Substituting Eq. (14) and Eq. (21), the partition function Z is,

$$Z = \sum_{i=1}^{N} \int \mathrm{d}\vec{r}_i \frac{\mathrm{e}^{-\beta N_i^+ (E_c + \Delta E)}\mathrm{e}^{-\beta N_i^- (E_c - \Delta E)}}{N_i^+! N_i^-!} \mathrm{e}^{-\beta W_i}. \tag{23}$$

In the remaining appendix, we focus on the partition function Eq. (23) to gain the thermodynamic properties of the model.

3) The boundary condition

The choice of boundary condition here for the two dimensional Coulomb gas is that the system has the conductor boundary. For the superconductor film, the electric current can't cross its boundary. In other words, the transverse part of the electric current density is equal to zero on the walls of the superconductor film,

$$\vec{j}_\perp(boundary) = 0. \tag{24}$$

Because of the $\vec{E} \perp \vec{j}$, the boundary condition corresponds to the two dimensional Coulomb gas is that of the longitudinal part of the electric intensity zero on the walls,

$$\vec{E}_{\parallel}(boundary) = 0, \tag{25}$$

which means that the model has the conductor boundary. Therefore, the potential φ on the boundary is constant according to electrostatics,

$$\varphi(boundary) = constant. \tag{26}$$

We deal with the influence of the boundary on the system by introducing mirror charges. According to the uniqueness theorem for Poisson's equation, the boundary effect is equivalent to so-called "mirror charges" only if they satisfy Poisson's equation and the same boundary condition. Mirror charges $q_i{}'$ must lie beyond the boundary, and are opposite to the original charges q_i. What's more, the potential $\varphi_i{}'(\vec{r})$ induced by a mirror charge has the same form as Eq. (11). Therefore, more comprehensively, the total potential $\varphi(\vec{r})$ can be expressed as,

$$\varphi(\vec{r}) = \sum_i \varphi_i(\vec{r}) + \sum_{i'} \varphi_i{}'(\vec{r}), \tag{27}$$

where the second term is mirror charges contribution. The position and quantity of mirror charges depend on the shape of the boundary. For the circular boundary of radius R, setting the center of the circle O as the origin, the position $\vec{r}_i{}'$ and quantity $q_i{}'$ of mirror charges for the two dimensional Coulomb gas are,

$$\begin{aligned} q_i{}' &= q_i, \\ r_i r_i{}' &= R^2, \end{aligned} \tag{28}$$

where q_i and $\vec{r}_i$ are the position and quantity of original charges, and $\vec{r}_i{}'$ is parallel to $\vec{r}_i$ (Fig. S9b).

4) The analytic method

In this section, we discuss the analytic method used here. We can obtain the thermodynamic properties of this two dimensional Coulomb gas model by calculating the partition function Eq. (23). However, Eq. (23) is too complex to gain the exact solution by calculating it analytically. One can also get the numerical solution of Eq. (23) by Monte Carlo methods [59]. Here, we adopt a simpler scheme described below to calculate Eq. (23). The partition function Eq. (23)

contains infinite sums over the number of particles so that we can't solve it directly. If the state of the system isn't close to the critical point, we can regard the fluctuations in the number of particles as the renormalization for the dielectric function ε [8]. In other words, the fluctuations can lead to the screening effect on the electric interactions between the particles, which can be described by ε. Therefore, by modifying the Coulomb potential Eq. (11) as,

$$\varphi_i(\vec{r}) = -\frac{1}{\varepsilon} q_i \ln\left(\frac{\vec{r}}{\lambda}\right), \tag{29}$$

we can keep only the first few terms (such as the first four terms) related to the particles with negative charges to calculate the partition function Z effortlessly. The dielectric function values at different temperatures can be obtained from the experiment.

We introduce the main procedures of the method as follows. In the following, we set the circular boundary of the system, and we chose units such that the charges of the particles $q_i = \pm 1$. Firstly, we express the partition function Z as,

$$\begin{aligned} Z = 1 + C_1 \mathrm{e}^{-\beta(E_c - \Delta E)} + \frac{C_2}{2} \mathrm{e}^{-2\beta(E_c - \Delta E)} \\ + \frac{C_3}{6} \mathrm{e}^{-3\beta(E_c - \Delta E)} + \frac{C_4}{24} \mathrm{e}^{-4\beta(E_c - \Delta E)}. \end{aligned} \tag{30}$$

The coefficients C_1, C_2, C_3, and C_4 are the following integrals

$$\begin{aligned} C_N &= \int \mathrm{d}\vec{r}\, \mathrm{e}^{-\beta W_N} \\ &= \int \mathrm{d}\vec{r}\, \mathrm{e}^{-\beta \frac{1}{2} \sum_{i=1}^{N} q_i \varphi(\vec{r}_i)} \\ &= \int \mathrm{d}\vec{r}\, \mathrm{e}^{-\beta \frac{1}{2} \sum_{i=1}^{N} q_i \left(\sum_{j=1}^{N} -\frac{1}{\varepsilon} q_j \ln\left(\frac{\vec{r}_i - \vec{r}_j}{\lambda}\right) + \sum_{j=1}^{N} -\frac{1}{\varepsilon} q_j{}' \ln\left(\frac{\vec{r}_i - \vec{r}_j{}'}{\lambda}\right)\right)}, \\ &(N = 1, 2, 3), \end{aligned} \tag{31}$$

where we use Eq. (23), Eq. (20), Eq. (27) and Eq. (29). We calculate the coefficients with Monte Carlo methods. Secondly, solve the free energy of the system taking advantage of Z,

$$F = -\frac{1}{\beta} \ln Z. \tag{32}$$

Finally, extract the magnetic susceptibility χ from the free energy according to thermodynamics,

$$\chi = -\frac{\partial^2 F}{\partial B^2}, \tag{33}$$

where B is the external magnetic field of the system. Substituting Eq. (15) to Eq. (33), the magnetic susceptibility χ is,

$$\chi = \frac{\partial^2 F}{\partial \Delta E^2}\frac{\partial^2 \Delta E}{\partial B^2}. \tag{34}$$

Plotting the magnetic susceptibility χ as a function of magnetic field B, we can get the $\chi'(T, H)$ as shown Fig. S10. Extracting the peak positions from this data, we obtained the $H_p(T)$ as shown in Fig. 3c. In this calculation, E_c and R, introduced in Sec. 3.2, are treated as free fitting parameters and obtained by fitting the location of the first two peaks at $T = 57$ K to the experimental data at the same temperature.

References for the Supplementary Materials

[56] L. D. Landau and E. M. Lifshitz, *Statistical physics*, v. 5. Course of Theoretical Physics, 23, 1980.

[57] S. Samuel, *Grand partition function in field theory with applications to sine-gordon field theory*, Physical Review D, 18(6):1916, 1978.

[58] P. Minnhagen, A Rosengren, and G Grinstein, *Screening properties of a classical two-dimensional coulomb gas from the sine-gordon equation*, Physical Review B, 18(3):1356, 1978.

[59] P. Minnhagen, *Kosterlitz-thouless transition for a two-dimensional superconductor: Magnetic-field dependence from a coulomb-gas analogy*, Physical Review B, 23(11):5745, 1981.

[60] J. Lidmar and M. Wallin, *Monte carlo simulation of a two-dimensional continuum coulomb gas*, Physical Review B, 55(1):522, 1997.

III. Figs. S1 to S10

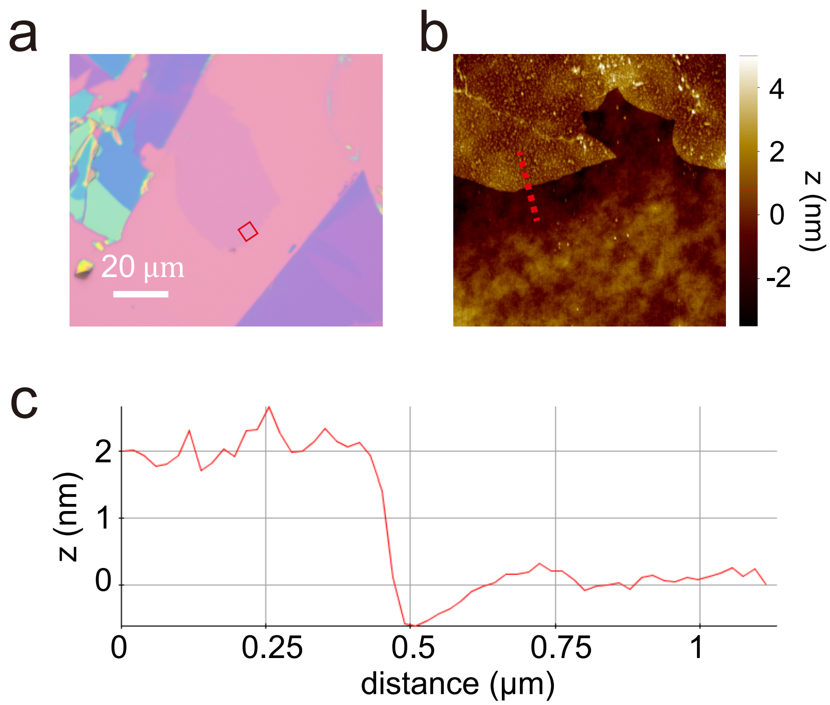

Fig. S1 Atomic force microscopy (AFM) image of a monolayer sample. **a**, Optical image of the sample. **b,** AFM image of the red box area in **a**. **c**, Line cut across the edge of the monolayer as labeled by the red line in **b**.

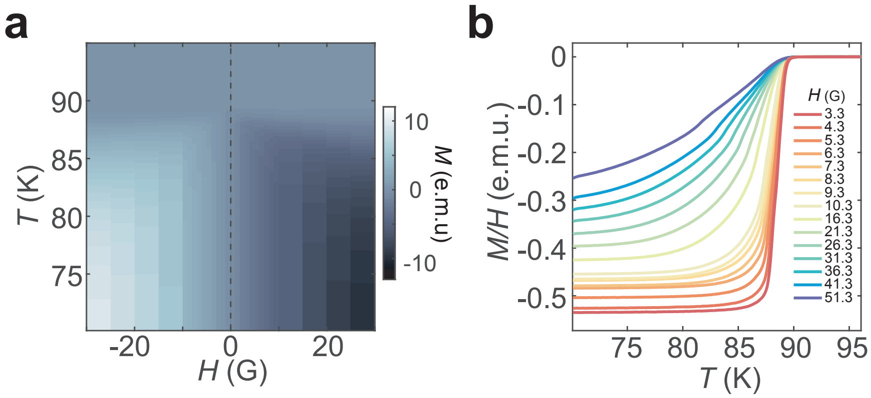

Fig. S2 Vibrating sample magnetometry of a bulk Bi2212 sample. a, Magnetization (*M*) as a function of temperature (*T*) and external perpendicular field (*H*). **b,** DC susceptibility as a function of *T* at various *H* obtained from **a** by *M*/*H*.

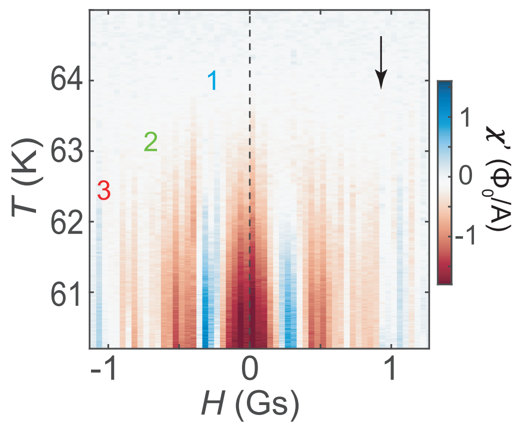

Fig. S3 Oscillating paramagnetic susceptibility in temperature sweeps of the monolayer sample. The data was obtained by fixing the field H and repeatedly cooling the sample through the transition temperature. The measurement location on the monolayer was labeled in **Fig. 1g** (the same location as that of the data in **Fig. 3a**.

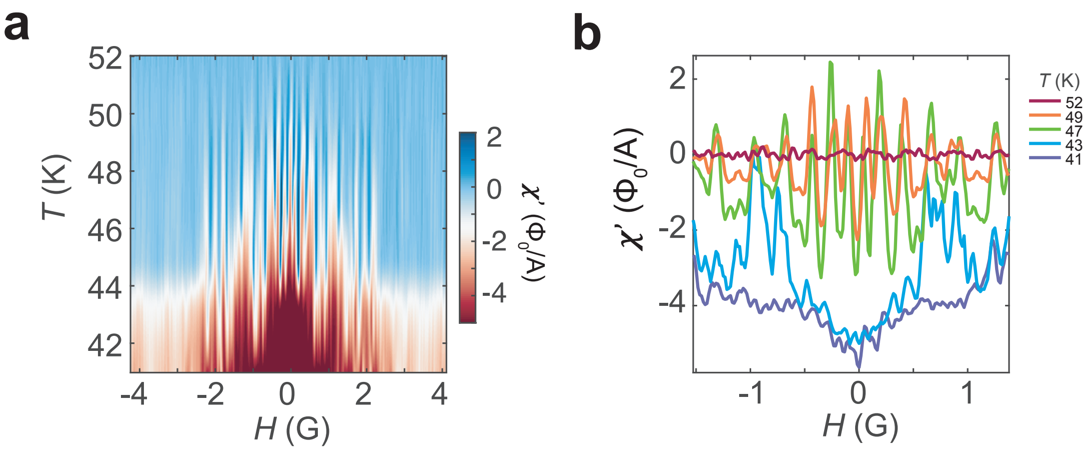

Fig. S4 Oscillating paramagnetic susceptibility of the monolayer sample at a different sample location. The measurement location was at the blue dot labeled in **Fig. 1g. a,** $\chi(T,H)'$ obtained by sweeping field at fixed temperature. **b,** $\chi(H)'$ at several T obtained from **a**. $T_{\mathrm{C}} = 52$ K at this domain.

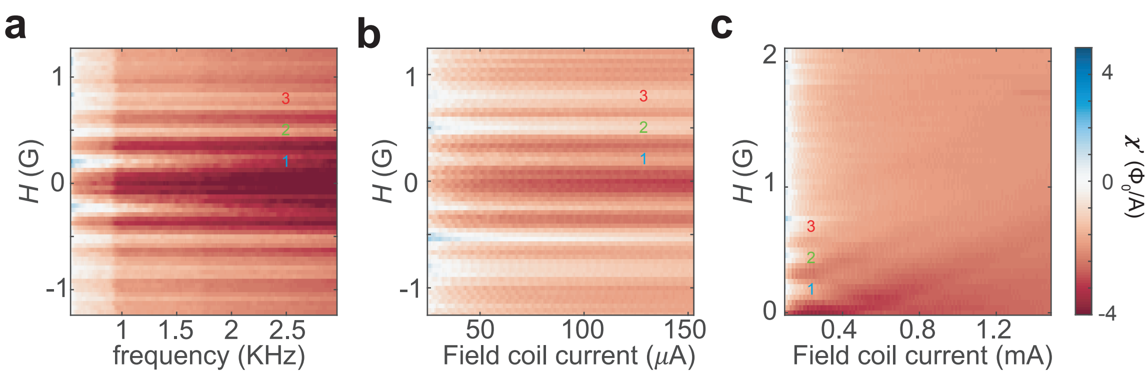

Fig. S5 Changing frequency and amplitude of the field coil modulation current. a, Susceptibility as a function of the alternating-current frequency through the field coil at various *H*. **b** and **c,** Susceptibility as a function of the driving amplitude through the field coil at various *H* for two different range of the amplitude, respectively. All the data were obtained at 60 K at the black dot on the monolayer as labeled in **Fig. 1g**. The paramagnetic peaks stayed constant with the driving frequency or the amplitude when the amplitude was small.

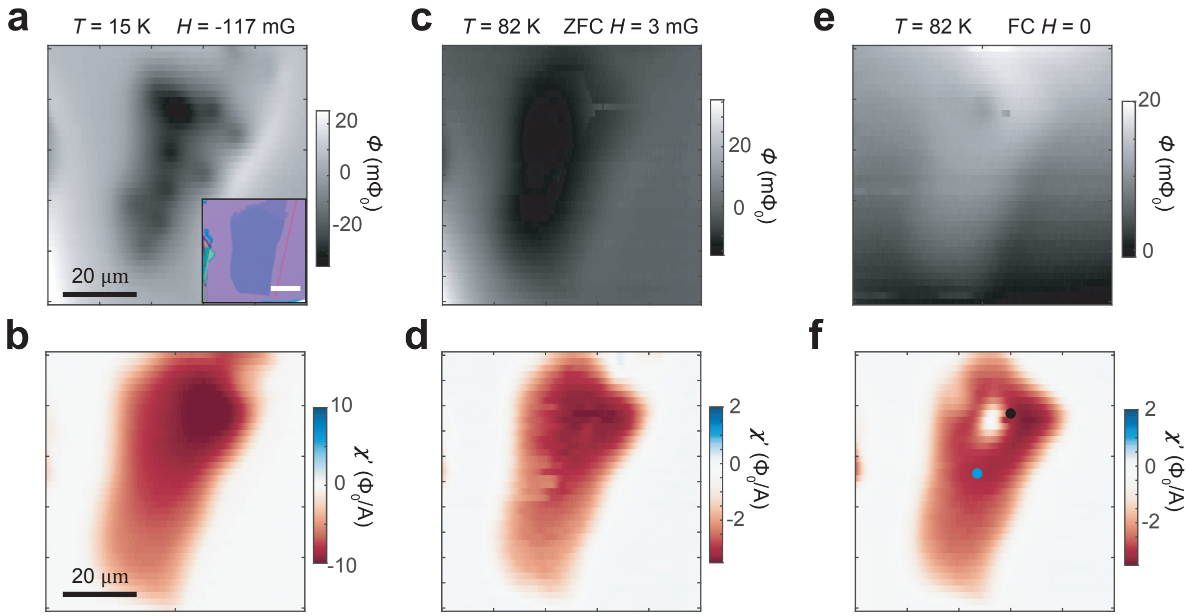

Fig. S6 sSQUID images of the Bi2212 quadruple-layer sample. a and **b**, Magnetometry and susceptometry images at $T = 15$ K and $H = -117$ mG. Inset: optical image of the sample. The white scale bar is 20 µm. **c** and **d**, Magnetometry and susceptometry images at $T = 82$ K and $H = 3$ mG after zero-field cooling. **e** and **f**, Magnetometry and susceptometry images at $T = 82$ K and $H = 0$. The sample was cooled under a small field so that a single vortex was trapped in the upper part of the sample. Data shown in **Figs. 4a** and **b** were obtained at the black point in **f**.

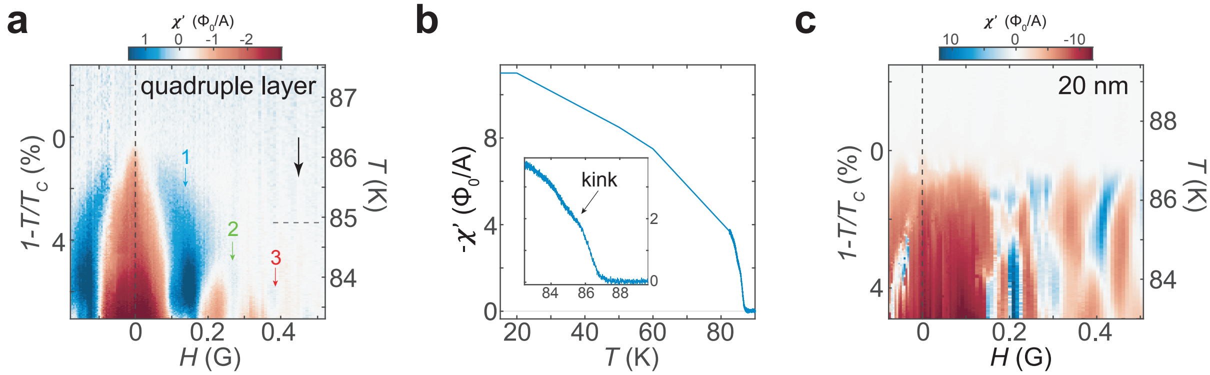

Fig. S7 Oscillating paramagnetic Meissner effect of the multilayer samples. a, $\chi(T,H)'$ of the quadruple layer sample obtained at the blue point shown in **Fig. S6f**. The gray dashed line separates the two temperature regions with (lower *T*) and without (higher *T*) interlayer coupling. The T_C of this area was slightly lower than that of the one shown in **Figure 4**. **b,** $-\chi(T)'$ at zero-field obtained from **a**. The inset shows a zoom in of the high temperature regime. The kink at 85 K was also visible at this location. **c,** $\chi(T,H)'$ of a 20 nm sample showing more sporadic PME behavior.

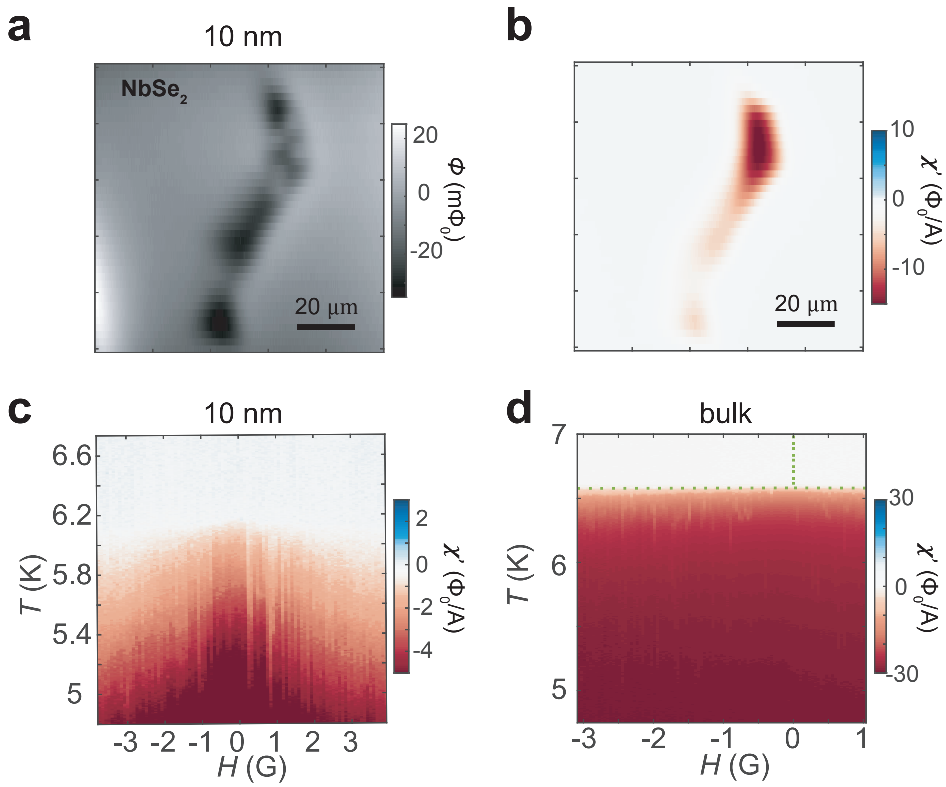

Fig. S8 sSQUID images of $NbSe_2$ samples. **a** and **b,** flux and χ' image of a 10-nm-thick $NbSe_2$ flake at 5 K. **c** and **d,** χ' of the 10-nm $NbSe_2$ flake and a bulk sample (at least 200 nm thick) as a function of *T* and *H* obtained by sweeping temperature at fixed field. The $\chi'(T)$ at zero-field of the bulk sample is shown in Fig. 4f. Even though the London penetration depth and coherence length of $NbSe_2$ are close to that of Bi2212, there are no observable paramagnetic susceptibility over a similar $\frac{T}{T_C} - H$ parameter space.

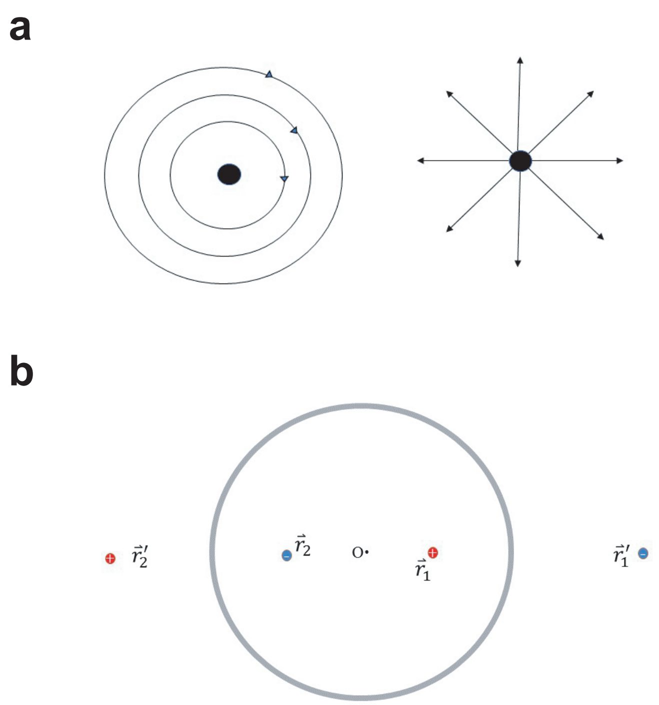

Fig. S9 Illustration of the Coulomb gas model. a, Sketch of the duality between the electric current density of a vortex (left) and the electric field produced by a charge (right). **b,** Sketch of mirror particles for a circular geometry. The grey circle is the sample boundary.

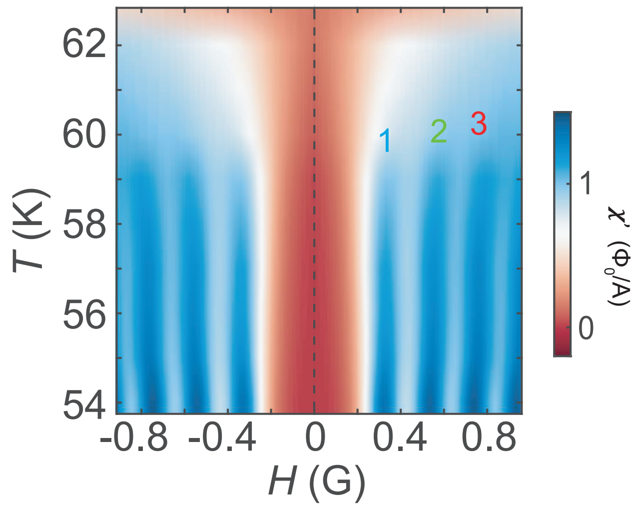

Fig. S10 Coulomb gas modeling of the PME oscillations. The simulated $\chi(T, H)'$ is for the monolayer sample shown in Fig. 3. The modeling was performed on the first four vortex entrance using the phase stiffness data acquired experimentally (Fig. 3c). The Meissner screening was ignored in the simulation (see text).